

Spin splitting of vortex beams on the surface ofnatural biaxial hyperbolic materials

Hong Liang(梁红), Haoyuan Song(宋浩元), Yubo Li(李宇博),Di Yu(于迪), and Shufang Fu(付淑芳)

Citation: Chin. Phys. B, 2023, 32 (**12**): 124212. DOI: 10.1088/1674-1056/ad0ccc
Journal homepage: http://cpb.iphy.ac.cn; http://iopscience.iop.org/cpb

What follows is a list of articles you may be interested in

Large spatial shifts of reflected light beam off biaxial hyperbolic materials

Jia-Guo Shen(沈加国), Syed-ul-hasnain Bakhtiar(哈思内恩), Hao-Yuan Song(宋浩元), Sheng Zhou(周胜), Shu-Fang Fu(付淑芳), Xuan-Zhang Wang(王选章), Xuan Wang(王暄), and Qiang Zhang(张强)
Chin. Phys. B, 2023, 32 (**11**): 114206. DOI: 10.1088/1674-1056/acd526

Ultraviolet metalens and metalens array of focused vortex beams

Jinping Zhang(张金平), Yan Wang(王焱), Huan Yuan(袁欢), Zehao Wang(王泽豪), Yang Deng(邓阳),Chengzhi Huang(黄承志), Jiagui Wu(吴加贵), and Junbo Yang(杨俊波)
Chin. Phys. B, 2023, 32 (**6**): 064206. DOI: 10.1088/1674-1056/ac9d87

Propagation and focusing characteristics of the Bessel-Gaussian beam with the spiral phase term of new power-exponent-phase

Aotian Wang(王傲天), Lianghong Yu(於亮红), Jinfeng Li(李进峰), and Xiaoyan Liang(梁晓燕)
Chin. Phys. B, 2023, 32 (**4**): 044201. DOI: 10.1088/1674-1056/acb1fe

Generation of elliptical airy vortex beams based on all-dielectric metasurface

Xiao-Ju Xue(薛晓菊), Bi-Jun Xu(徐弼军), Bai-Rui Wu(吴白瑞), Xiao-Gang Wang(汪小刚), Xin-Ning Yu(俞昕宁), Lu Lin(林露), and Hong-Qiang Li(李宏强)
Chin. Phys. B, 2023, 32 (**2**): 024215. DOI: 10.1088/1674-1056/ac7cd0

Plasmon-phonon coupling in graphene-hyperbolic bilayer heterostructures

Ge Yin(尹格), Jun Yuan(元军), Wei Jiang(姜玮), Jianfei Zhu(朱剑飞), Yungui Ma(马云贵)
Chin. Phys. B, 2016, 25 (**11**): 114216. DOI: 10.1088/1674-1056/25/11/114216

Spin splitting of vortex beams on the surface of natural biaxial hyperbolic materials

Hong Liang(梁红)[1], Haoyuan Song(宋浩元)[2], Yubo Li(李宇博)[2], Di Yu(于迪)[2], and Shufang Fu(付淑芳)[2,†]

[1] *Department of Physics, Harbin University, Harbin* 150086, *China*
[2] *Key Laboratory for Photonic and Electronic Bandgap Materials, Ministry of Education, School of Physics and Electronic Engineering, Harbin Normal University, Harbin* 150025, *China*

(Received 22 September 2023; revised manuscript received 5 November 2023; accepted manuscript online 16 November 2023)

We investigated the spin splitting of vortex beam on the surface of biaxial natural hyperbolic materials (NHMs) rotated by an angle with respect to the incident plane. An obvious asymmetry of spatial shifts produced by the left-handed circularly (LCP) component and right-handed circularly polarized (RCP) component is exhibited. We derived the analytical expression for in- and out-of-plane spatial shifts for each spin component of the vortex beam. The orientation angle of the optical axis plays a key role in the spin splitting between the two spin components, which can be reflected in the simple expressions for spatial shifts without the rotation angle. Based on an α-MoO_3 biaxial NHM, the spatial shifts of the two spin components with the topological charge were investigated. As the topological charge increases, the spatial shifts also increase; in addition, a tiny spatial shift close to zero can be obtained if we control the incident frequency or the polarization of the reflected beams. It can also be concluded that the maximum of the spin splitting results from the LCP component at p-incidence and the RCP component at s-incidence in the RB-II hyperbolic frequency band. The effect of the incident angle and the thickness of the α-MoO_3 film on spin splitting is also considered. These results can be used for manipulating infrared radiation and optical detection.

Keywords: spin splitting, hyperbolic material, vortex beam, orbital angular momentum

PACS: 42.25.Gy, 41.85.Ct, 78.20.–e, 78.68.+m **DOI:** 10.1088/1674-1056/ad0ccc

1. Introduction

A polarization-dependent spatial shift in both in- and out-of-plane directions is generated when linearly polarized light combining a left-handed circularly polarized (LCP) component and a right-handed circularly polarized (RCP) component refracts or reflects at a dielectric interface; this was defined as the spin Hall effect (SHE) of light by Onoda *et al.* in 2004.[1] In 2006, Bliokh *et al.* interpreted this concept and proposed that the conservation of total angular momentum is necessary.[2] It is well known that photons with two different spins in linearly polarized light carry different spin angular momenta. Generation of the SHE can compensate the extrinsic orbital angular momentum of different spin states to guarantee the conservation of angular momentum after reflection and refraction at the surface of materials. The SHE has attracted much attention and been applied in the development of new nanophotonic devices, such as plasmonics,[3,4] hyperbolic metamaterials (MMs),[5] topological insulators,[6] graphene,[7,8] black phosphorus,[9] and so on.

Recently, a variety of spatially structured beams with novel properties, such as vortex beams,[10] Airy beams[11] and Bessel beams,[12] have emerged, which provide a new path for studying the tunable SHE. A vortex beam with a continuous spiral phase and a vortex center phase singularity carries the orbital angular momentum and phase singularity.[13] Due to the consideration of orbital angular momentum, vortex beams have been widely used in optical communication,[14] trapping[15] and optical microscopy.[16] The spatial shifts of LCP and RCP components could be significantly enhanced with increase in the topological charge, which leads to the opportunity to observe the shifts directly.[17–19] Normally, the spin splitting produced by linearly polarized light is symmetric, i.e., the position and intensity of the shifts of RCP and LCP components are equally separated. However, the asymmetry of spin splitting is also an interesting phenomenon, showing the powerful ability for multi-dimensional and flexible control of spin photons.[20] A vortex beam can be used to excite asymmetric spin splitting and has been widely studied in various systems such as graphene metamaterials,[17] an air–gold interface,[18] PT-symmetric metamaterials,[19] etc.

Hyperbolic metamaterials (HMMs), a class of artificial electromagnetic metamaterials, have been widely used in many fields due to their strong anisotropy and hyperbolic dispersion, for example in super-resolution imaging,[21,22] negative refraction,[23] optical waveguides[24,25] and ultra-sensitive optical sensing.[26] In contrast to HMMs, natural hyperbolic materials (NHMs), represented by hexagonal boron nitride (hBN) and alpha-phase molybdenum trioxide (α-MoO_3), exhibit lower optical losses and are easy to prepare and highly stable.[27] In recent years, due to its in-plane anisotropy char-

†Corresponding author. E-mail: shufangfu75@163.com

© 2023 Chinese Physical Society and IOP Publishing Ltd

acteristics and excellent energy storage performance, α-MoO_3 has received widespread attention.[28–30] Compared with other hyperbolic materials, α-MoO_3 has two main advantages: one is that the hyperbolic frequency interval of α-MoO_3 is wider. For example, for the c-axis ([001] crystal direction) the hyperbolic frequency interval of α-MoO_3 is three times that of hBN, which will be beneficial for broadband modulation of electromagnetic waves.[31,32] The other one is that α-MoO_3 has three different hyperbolic frequency bands (RBs), and each RB corresponds to a different crystal axis, making it possible to achieve a hyperbolic surface in the plane.[31,32] Recently, Wang *et al.* studied the spin splitting of vortex beams irradiated on semi-infinite uniaxial natural hBN.[33] It was found that the spin splitting is significant when the Brewster angle or critical angle is satisfied, and the spin splitting can be enhanced by intrinsic orbital angular momentum. In contrast to hBN, the anisotropy of α-MoO_3 films is stronger, which is attributed to their biaxial hyperbolic character. Meanwhile, the RBs of α-MoO_3 are continuous from 545 cm^{-1} to 1004 cm^{-1} and overlap at the adjacent regions, which are wider than the separated ones of hBN. On the other hand, a rotation angle between the crystal direction of α-MoO_3 and the incident plane is set, which will result in obvious asymmetry of spin splitting between LCP and RCP components. However, for the spin splitting of hBN, a pronounced asymmetry will emerge when the polarization angle $\alpha \neq 0°$ and 90°.

In this work, we focus on the SHE of a reflected vortex beam on the surface of α-MoO_3 rotated by an angle with respect to the incident plane for differently polarized beams. The enhanced shifts can be realized by adjusting the corresponding physical parameters, such as the topological charge, and apparent asymmetry of spin splitting is observed. The organization of this article is as follows. In Section 2, the analytical expressions for in- or out-of-plane spatial shifts are derived. The spin splitting between LCP and RCP components is defined. The analysis corresponding to the spin splitting and the spatial shifts of LCP and RCP components under the effect of orientation angle, incident angle and the thickness of α-MoO_3, as well as the topological charge, is given Section 3. Finally, Section 4 summarizes the useful conclusions of this paper.

2. Theoretical description

The coordinate system and schematic diagram are shown in Fig. 1(a). The principal axis coordinate system [a, b, c] represents the [100], [010] and [001] crystal directions, respectively, of α-MoO_3 with thickness d. The a- and c-axes of α-MoO_3 are in the x–y plane of the experimental coordinate system. The a-axis is rotated by an angle φ relative to the x-axis, which also represents the direction of the incident plane. A vortex beam is incident on the surface at an angle θ in the x–z plane. The reflected beam splits along the x- and y-axes and produces the in- and out-of-plane spin splittings, respectively. Figure 1(b) represents the real parts of the α-MoO_3 permittivity, where the RBs are shown between epsilon-near-zero (ENZ) and epsilon-near-pole (ENP). In the principal axis coordinate system, the permittivity of α-MoO_3 can be written as a diagonal matrix [ε_x, ε_y, ε_z]. The components of permittivity can be collectively expressed by[35]

$$\varepsilon_j = \varepsilon_{\infty,j}\left(1+\frac{f_{\mathrm{LO},j}^2 - f_{\mathrm{TO},j}^2}{f_{\mathrm{TO},j}^2 - f^2 - \mathrm{i}f\tau_j}\right), \quad (j=x,y,z), \tag{1}$$

where ε_∞ is the high-frequency dielectric constant, f_{TO} and f_{LO} indicate the transverse and longitudinal optical phonon frequencies and τ_j is the phonon-damping constant. In Eq. (1), the frequency is generally measured in cm^{-1} so that f actually represents $\omega/(2\pi c)$. The regions with negative values of permittivity along all three directions correspond to the hyperbolic frequency range. The frequency region 545 $cm^{-1} < f <$ 851 cm^{-1} is defined as RBI, where $\varepsilon_y < 0$; within the range 822 $cm^{-1} < f <$ 972 cm^{-1}, the hyperbolic frequency range is defined as RBII, where $\varepsilon_x < 0$; and within the range 958 $cm^{-1} < f <$ 1004 cm^{-1}, the hyperbolic frequency range with $\varepsilon_z < 0$ is RBIII. In fact, some overlapping areas exist between the boundaries of the RBs, as described by Fig. 1(b). For example, in the overlapping area of RB-I and RB-II, it can be found that $\varepsilon_x < \varepsilon_y < 0$, while in the overlapping area of RB-II and RB-III, the permittivity satisfies $\varepsilon_z < \varepsilon_x < 0$.

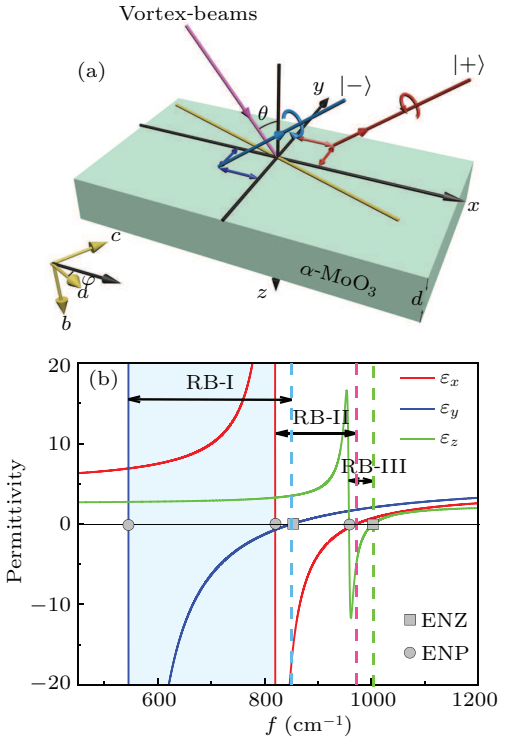


Fig. 1. The left graph illustrates the spin splitting of a reflected vortex beam from the surface of an α-MoO_3 film with thickness d. The incident plane is the x–z plane. The red and blue rotating arrows represent the reflected LCP and RCP components, respectively. [a, b, c] represents the principal axis coordinate system and is rotated by φ with respect to the incident plane. The right graph illustrates the real parts of permittivity of α-MoO_3.

Since an angle φ is set between the a-axis and the x-axis, a coordinate transformation is required. The equivalent matrix of permittivity can be written as[36]

$$\varepsilon = \varepsilon_0 \begin{pmatrix} \varepsilon_{xx} & \varepsilon_{xy} & 0 \\ \varepsilon_{xy} & \varepsilon_{yy} & 0 \\ 0 & 0 & \varepsilon_{zz} \end{pmatrix}, \tag{2}$$

where $\varepsilon_{xx} = \varepsilon_x \cos^2\varphi + \varepsilon_y \sin^2\varphi$, $\varepsilon_{yy} = \varepsilon_y \cos^2\varphi + \varepsilon_x \sin^2\varphi$, $\varepsilon_{zz} = \varepsilon_z$ and $\varepsilon_{xy} = (\varepsilon_y - \varepsilon_x)\cos\varphi\sin\varphi$. With the Maxwell equation, three components of electric fields satisfy the following relationship:

$$\begin{pmatrix} k_z - \varepsilon_{xx} f^2 & -\varepsilon_{xy} f^2 & k_x k_z \\ -\varepsilon_{xy} f^2 & k_x^2 + k_z^2 - \varepsilon_{yy} f^2 & 0 \\ k_x k_z & 0 & k_x^2 - \varepsilon_z f^2 \end{pmatrix} \begin{pmatrix} E_x \\ E_y \\ E_z \end{pmatrix} = 0. \tag{3}$$

According to Cramer's rule, when the determinant of the coefficient matrix is zero, the equation has a solution. In this case, Eq. (3) leads to a quadratic equation with respect to the wave vector. Then, using the quadratic formula, we have

$$k_\pm^2 = \frac{1}{2\varepsilon_z}(-a \pm \sqrt{a^2 - 4\varepsilon_z b}), \tag{4}$$

with $a = \varepsilon_{xx}(k_x^2 - \varepsilon_z f^2) + \varepsilon_z(k_x^2 - \varepsilon_{yy} f^2)$ and $b = \left(k_x^2 - \varepsilon_z f^2\right)\left(\varepsilon_{xx} k_x^2 - \varepsilon_{xx}\varepsilon_{yy} f^2 + \varepsilon_{xy}^2 f^2\right)$. $k_\pm$ represents the two wave vectors of the z-component in α-MoO_3 film. Incident and transmitted wave vectors can be expressed as $k_x = f\sin\theta$, $k_z = f\cos\theta$. The reflected wave vector is $-k_z$. From Eq. (3), the electric fields components along the x- and z-directions can be expressed as a function of electric field component along the y-direction

$$E_x^\pm = \frac{k_x^2 + k_\pm^2 - \varepsilon_{yy} f^2}{\varepsilon_{xy} f^2} E_y^\pm = \Lambda_\pm E_y^\pm, \tag{5a}$$

$$E_z^\pm = \frac{k_\pm k_x \Lambda_\pm}{\varepsilon_z f^2 - k_x^2} E_y^\pm. \tag{5b}$$

Hence, we propose only the y-component of electric field in the α-MoO_3 film, but the x- and y-components in the other spaces as follows:

$$E_{x,y} = \left(E_{x,y}^{\mathrm{i}} e^{\mathrm{i}k_z z} + E_{x,y}^{\mathrm{r}} e^{-\mathrm{i}k_z z}\right) e^{\mathrm{i}k_x x - \mathrm{i}\omega t}, \quad (z < 0), \tag{6a}$$

$$E_y = \left(A e^{\mathrm{i}k_+ z} + B e^{-\mathrm{i}k_+ z} + C e^{\mathrm{i}k_- z} + D e^{-\mathrm{i}k_- z}\right) e^{\mathrm{i}k_x x - \mathrm{i}\omega t}, \quad (0 < z < d), \tag{6b}$$

$$E_x = F_x e^{\mathrm{i}k_z z + \mathrm{i}k_x x - \mathrm{i}\omega t}, \quad E_y = F_y e^{\mathrm{i}k_z z + \mathrm{i}k_x x - \mathrm{i}\omega t}, \quad (z > d). \tag{6c}$$

In different spaces, the magnetic fields can be obtained from $\boldsymbol{H} = \nabla \times \boldsymbol{E}/(\mathrm{i}\mu_0\omega)$. Then, at the upper surface of the α-MoO_3 film, the electromagnetic boundary conditions can be written as

$$E_y^{\mathrm{i}} + E_y^{\mathrm{r}} = A + B + C + D, \tag{7a}$$

$$E_y^{\mathrm{i}} - E_y^{\mathrm{r}} = \left[k_+ (A - B) + k_- (C - D)\right]/k_z, \tag{7b}$$

$$E_x^{\mathrm{i}} + E_x^{\mathrm{r}} = \Lambda_+ (A + B) + \Lambda_- (C + D), \tag{7c}$$

$$E_y^{\mathrm{i}} - E_y^{\mathrm{r}} = \lambda_+ (A - B) + \lambda_- (C - D), \tag{7d}$$

where $\lambda_\pm = k_\pm k_0 \varepsilon_z \Lambda_\pm/(\varepsilon_z f^2 - k_x^2)$. At the lower interface between the α-MoO_3 film and the air, we find

$$A e^{\mathrm{i}k_+ d} + B e^{-\mathrm{i}k_+ d} + C e^{\mathrm{i}k_- d} + D e^{-\mathrm{i}k_- d} = F_y, \tag{8a}$$

$$k_+ (A e^{\mathrm{i}k_+ d} - B e^{-\mathrm{i}k_+ d}) + k_- (C e^{\mathrm{i}k_- d} - D e^{-\mathrm{i}k_- d}) = k_z F_y, \tag{8b}$$

$$\Lambda_+ (A e^{\mathrm{i}k_+ d} + B e^{-\mathrm{i}k_+ d}) + \Lambda_- (C e^{\mathrm{i}k_- d} + D e^{-\mathrm{i}k_- d}) = F_x, \tag{8c}$$

$$\gamma_+ (A e^{\mathrm{i}k_+ d} - B e^{-\mathrm{i}k_+ d}) + \gamma_- (C e^{\mathrm{i}k_- d} - D e^{-\mathrm{i}k_- d}) = F_x, \tag{8d}$$

where $\gamma_\pm = k_\pm f \varepsilon_z \Lambda_\pm/(\varepsilon_z f^2 - k_x^2)$. For convenience, we transform Eqs. (7) and (8) into matrix forms as follows:

$$\begin{pmatrix} E_y^{\mathrm{i}} \\ E_y^{\mathrm{r}} \\ E_x^{\mathrm{i}} \\ E_x^{\mathrm{r}} \end{pmatrix} = \frac{1}{2} \begin{pmatrix} 1 + k_+/k_z & 1 - k_+/k_z & 1 + k_-/k_z & 1 - k_-/k_z \\ 1 - k_+/k_z & 1 + k_+/k_z & 1 - k_-/k_z & 1 + k_-/k_z \\ \Lambda_+ + \lambda_+ & \Lambda_+ - \lambda_+ & \Lambda_- + \lambda_- & \Lambda_- - \lambda_- \\ \Lambda_+ - \lambda_+ & \Lambda_+ + \lambda_+ & \Lambda_- - \lambda_- & \Lambda_- + \lambda_- \end{pmatrix} \begin{pmatrix} A \\ B \\ C \\ D \end{pmatrix} = T_1 \begin{pmatrix} A \\ B \\ C \\ D \end{pmatrix}, \tag{9a}$$

$$\begin{pmatrix} F_y \\ 0 \\ F_x \\ 0 \end{pmatrix} = \begin{pmatrix} (1 + k_+/k_z) p_+^+ & (1 - k_+/k_z) p_-^- & (1 + k_-/k_z) p_-^+ & (1 - k_-/k_z) p_-^- \\ (1 - k_+/k_z) p_+^+ & (1 + k_+/k_z) p_+^- & (1 - k_-/k_z) p_-^+ & (1 + k_-/k_z) p_-^- \\ (\Lambda_+ + \gamma_+) p_+^+ & (\Lambda_+ - \gamma_+) p_+^- & (\Lambda_- + \gamma_-) p_-^+ & (\Lambda_- - \gamma_-) p_-^- \\ (\Lambda_+ - \gamma_+) p_+^+ & (\Lambda_+ + \gamma_+) p_+^- & (\Lambda_- - \gamma_-) p_-^+ & (\Lambda_- + \gamma_-) p_-^- \end{pmatrix} \begin{pmatrix} A \\ B \\ C \\ D \end{pmatrix} = T_2 \begin{pmatrix} A \\ B \\ C \\ D \end{pmatrix}, \tag{9b}$$

where $p_\pm^\pm = \exp(\pm \mathrm{i}k_\pm d)$. Combining the two matrices of Eqs. (9a) and (9b), we eliminate the electric field amplitudes A, B, C and D to obtain the relationship between incident, reflected and transmitted electric fields

$$\begin{pmatrix} E_y^{\mathrm{i}} \\ E_y^{\mathrm{r}} \\ E_x^{\mathrm{i}} \\ E_x^{\mathrm{r}} \end{pmatrix} = T \begin{pmatrix} F_y \\ 0 \\ F_x \\ 0 \end{pmatrix}, \tag{10}$$

where $T = T_1 T_2^{-1}$. According to Eq. (10), the relationship between incident and reflected fields can be obtained as

$$E_y^{\rm r} = \frac{t_{21}t_{33} - t_{23}t_{31}}{t_{11}t_{33} - t_{13}t_{31}} E_y^{\rm i} + \frac{t_{11}t_{23} - t_{21}t_{13}}{t_{11}t_{33} - t_{13}t_{31}} E_x^{\rm i}, \tag{11a}$$

$$E_x^{\rm r} = \frac{t_{41}t_{33} - t_{43}t_{31}}{t_{11}t_{33} - t_{13}t_{31}} E_y^{\rm i} + \frac{t_{11}t_{43} - t_{41}t_{13}}{t_{11}t_{33} - t_{13}t_{31}} E_x^{\rm i}, \tag{11b}$$

where t_{ij} represents the elements of matrix T. The z-component of the reflective electric field is $E_z^{\rm r} = \tan\theta E_x^{\rm r}$. For the reflective beam, $E_y^{\rm r}$ denotes the component of the s-wave (TE-wave), while $E_x^{\rm r}$ and $E_z^{\rm r}$ are the components that make up the p-wave (TM-wave). In order to explain the spin splitting, it is necessary to obtain the matrix expression for the reflective electric field in the xyz coordinate system. Then, Eq. (11) is changed into a matrix expression,[36] i.e.,

$$\begin{pmatrix} E_{\rm p}^{\rm r} \\ E_{\rm s}^{\rm r} \end{pmatrix} = \begin{pmatrix} -a_{11} & -a_{12}/\cos\theta \\ a_{21}\cos\theta & a_{22} \end{pmatrix} \begin{pmatrix} E_{\rm p}^{\rm i} \\ E_{\rm s}^{\rm i} \end{pmatrix} = \begin{pmatrix} r_{\rm pp} & r_{\rm ps} \\ r_{\rm sp} & r_{\rm ss} \end{pmatrix} \begin{pmatrix} E_{\rm p}^{\rm i} \\ E_{\rm s}^{\rm i} \end{pmatrix}, \tag{12}$$

with

$$a_{11} = \frac{t_{11}t_{43} - t_{41}t_{13}}{t_{11}t_{33} - t_{13}t_{31}}, \quad a_{12} = \frac{t_{41}t_{33} - t_{43}t_{31}}{t_{11}t_{33} - t_{13}t_{31}}, \tag{13a}$$

$$a_{21} = \frac{t_{11}t_{23} - t_{21}t_{13}}{t_{11}t_{33} - t_{13}t_{31}}, \quad a_{22} = \frac{t_{21}t_{33} - t_{23}t_{31}}{t_{11}t_{33} - t_{13}t_{31}}. \tag{13b}$$

The incident beam, as a near-axial beam, has a narrow plane wave distribution along the center wave in momentum space. If μ and ν indicate the in-plane and out-of-plane deflections of non-central wave vectors, respectively, the reflective electric field components can be rewritten with the angular spectrum theory for the ordinary situation[36,37]

$$\begin{pmatrix} E_{\rm r}^{\rm H} \\ E_{\rm r}^{\rm V} \end{pmatrix} = \begin{pmatrix} r_{\rm pp} - \mu\frac{\partial r_{\rm pp}}{\partial\theta} - \nu[(r_{\rm ps} - r_{\rm sp})\cot\theta + \frac{\partial r_{\rm pp}}{\partial\varphi}] & r_{\rm ps} - \mu\frac{\partial r_{\rm ps}}{\partial\theta} + \nu[(r_{\rm pp} + r_{\rm ss})\cot\theta - \frac{\partial r_{\rm ps}}{\partial\varphi}] \\ r_{\rm sp} - \mu\frac{\partial r_{\rm sp}}{\partial\theta} - \nu[(r_{\rm pp} + r_{\rm ss})\cot\theta + \frac{\partial r_{\rm sp}}{\partial\varphi}] & r_{\rm ss} - \mu\frac{\partial r_{\rm ss}}{\partial\theta} + \nu[(r_{\rm sp} - r_{\rm ps})\cot\theta - \frac{\partial r_{\rm ss}}{\partial\varphi}] \end{pmatrix} \begin{pmatrix} E_{\rm i}^{\rm H} \\ E_{\rm i}^{\rm V} \end{pmatrix} = {\rm F} \begin{pmatrix} E_{\rm i}^{\rm H} \\ E_{\rm i}^{\rm V} \end{pmatrix}, \tag{14}$$

where the terms related to μ denote the in-plane momentum gradient of the Fresnel coefficients and the terms related to ν denote the geometric spin–orbit terms.

For convenience, we use a simple vortex beam as the incident beam to simulate the spin-splitting. The simple vortex beam is equal to the first-order Laguerre–Gaussian beam whose radial index is equal to zero and its envelope does not depend on the radial coordinate at all. The angular distribution of electric field is explicitly expressed by[33,36]

$$\begin{aligned} E^0(\mu,\nu) &= \frac{w_0}{\sqrt{2\pi}} \left[\frac{w_0 k_0}{\sqrt{2}}(-{\rm i}\mu + {\rm sgn}[m]\nu)\right]^{|m|} \\ &\quad \times \exp\left[-\frac{k_0^2 w_0^2}{4}(\mu^2 + \nu^2)\right], \end{aligned} \tag{15}$$

where m is the azimuthal quantum number characterizing the optical vortex and its sign indicates the direction of the vortex. w_0 is the width of the beam waist and k_0 is the vacuum wave number. The field amplitude components corresponding to any branch wave in the reflected beam can be expressed as

$$\begin{pmatrix} E_{\rm r}^{\rm H} \\ E_{\rm r}^{\rm V} \end{pmatrix} = E^0(\mu,\nu) F \begin{pmatrix} E_{\rm i}^{\rm H} \\ E_{\rm i}^{\rm V} \end{pmatrix}. \tag{16}$$

In the spin basis set, the incident beam can be rewritten as the superposition of the LCP and RCP components, i.e., $|E_{\rm r}^{\rm H}\rangle = (|e_+^{\rm r}\rangle + |e_-^{\rm r}\rangle)/\sqrt{2}$, $|E_{\rm r}^{\rm V}\rangle = -{\rm i}(|e_+^{\rm r}\rangle - |e_-^{\rm r}\rangle)/\sqrt{2}$. $|e_+^{\rm r}\rangle$ and $|e_-^{\rm r}\rangle$ represent the LCP and RCP components, respectively. Therefore, the reflective matrix (15) can be rewritten as

$$\begin{aligned} |E_\pm^{\rm r}\rangle &= E^0(\mu,\nu)\frac{1}{\sqrt{2}}(F_{11}E_{\rm i}^{\rm H} + F_{12}E_{\rm i}^{\rm V} \\ &\quad \mp {\rm i}F_{21}E_{\rm i}^{\rm H} \mp {\rm i}F_{22}E_{\rm i}^{\rm V})\,|e_\pm^{\rm r}\rangle \\ &= E^0(\mu,\nu)[O_\pm + P_\pm\mu + Q_\pm\nu]\,|e_\pm^{\rm r}\rangle, \end{aligned} \tag{17}$$

with

$$O_\pm = r_{\rm pp}E_{\rm i}^{\rm H} + r_{\rm ps}E_{\rm i}^{\rm V} \mp {\rm i}r_{\rm sp}E_{\rm i}^{\rm H} \mp {\rm i}r_{\rm ss}E_{\rm i}^{\rm V}, \tag{18a}$$

$$P_\pm = \frac{\partial r_{\rm pp}}{\partial\theta}E_{\rm i}^{\rm H} + \frac{\partial r_{\rm ps}}{\partial\theta}E_{\rm i}^{\rm V} \mp {\rm i}\frac{\partial r_{\rm sp}}{\partial\theta}E_{\rm i}^{\rm H} \mp {\rm i}\frac{\partial r_{\rm ss}}{\partial\theta}E_{\rm i}^{\rm V}, \tag{18b}$$

$$\begin{aligned} Q_\pm = \Bigg\{ &\left[-(r_{\rm ps} - r_{\rm sp})\cot\theta + \frac{\partial r_{\rm pp}}{\partial\varphi}\right]E_{\rm i}^{\rm H} \\ &+ \left[(r_{\rm pp} + r_{\rm ss})\cot\theta - \frac{\partial r_{\rm ps}}{\partial\varphi}\right]E_{\rm i}^{\rm V} \\ &\mp {\rm i}\left[-(r_{\rm pp} + r_{\rm ss})\cot\theta + \frac{\partial r_{\rm sp}}{\partial\varphi}\right]E_{\rm i}^{\rm H} \\ &\mp {\rm i}\left[(r_{\rm sp} - r_{\rm ps})\cot\theta - \frac{\partial r_{\rm ss}}{\partial\varphi}\right]E_{\rm i}^{\rm V}\Bigg\}, \end{aligned} \tag{18c}$$

where F_{ij} represents the elements of matrix F, $O_\pm$ represents the terms regardless of μ and ν, $P_\pm$only includes μ and omits ν and $Q_\pm$ only includes ν and omits μ. Therefore, the spatial shifts of either spin-state component can be defined as[36]

$$\langle x_\pm\rangle = -\frac{\langle E_\pm^{\rm r}|\,\frac{{\rm i}\partial}{k\partial\mu}\,|E_\pm^{\rm r}\rangle}{\langle E_\pm^{\rm r}|\,|E_\pm^{\rm r}\rangle}, \quad \langle y_\pm\rangle = \frac{\langle E_\pm^{\rm r}|\,\frac{{\rm i}\partial}{k\partial\nu}\,|E_\pm^{\rm r}\rangle}{\langle E_\pm^{\rm r}|\,|E_\pm^{\rm r}\rangle}. \tag{19}$$

Taking Eq. (18) into Eq. (19), we have

$$\langle x_\pm\rangle = -\frac{1}{k_0}\frac{me_{3\pm} + {\rm i}2f_{1\pm}}{2e_{1\pm} + (e_{4\pm} + e_{5\pm})\left(\frac{2}{k^2w_0^2}\right)(m+1)}, \tag{20a}$$

$$\langle y_\pm\rangle = \frac{1}{k_0}\frac{me_{2\pm} + {\rm i}2f_{2\pm}}{2e_{1\pm} + (e_{4\pm} + e_{5\pm})\left(\frac{2}{k^2w_0^2}\right)(m+1)}. \tag{20b}$$

Here $e_{1\pm} = |O_\pm|^2$, $e_{2\pm} = O_\pm^* P_\pm + P_\pm^* O_\pm$, $e_{3\pm} = O_\pm^* Q_\pm + Q_\pm^* O_\pm$, $e_{4\pm} = |P_\pm|^2$, $e_{5\pm} = |Q_\pm|^2$, $f_{1\pm} = O_\pm^* P_\pm$, and $f_{2\pm} = O_\pm^* Q_\pm$. $\Delta xy = \langle x_+,\ y_+\rangle - \langle x_-,\ y_-\rangle$ is the shift difference between LCP and RCP components, i.e., the spin splitting.[30] When $e_{1\pm} \gg (m+1)(e_{4\pm}+e_{5\pm})/(k^2 w_0^2)$, the second term of the numerator in Eqs. (20a) and (20b) represents the primordial shifts which are caused by the Gaussian beams. The first term represents the dependence on the intrinsic orbit angular momentum, which results in the linear increase of the spatial shifts with increase in the azimuthal quantum number. If $e_{1\pm} \ll (m+1)(e_{4\pm}+e_{5\pm})/(k^2 w_0^2)$, the beam shifts tend to zero due to $|O_\pm| \ll |P_\pm|$ and $|O_\pm| \ll |Q_\pm|$. When $e_{1\pm}$ is of the same order of magnitude as $(m+1)(e_{4\pm}+e_{5\pm})/(k^2 w_0^2)$, the effect of the topological charge number on the spin splitting becomes more complex. If we replace α-MoO_3 with an isotropic medium, the effect of orientation angle φ on the permittivity matrix will disappear, which causes the reflection coefficient $r_{ps} = r_{sp} = 0$. In this case, Eq. (17) can be transformed as

$$E_r^{\pm} = \frac{1}{\sqrt{2}}\left[r_{pp} - \mu\frac{\partial}{\partial\theta} r_{pp} \pm \mathrm{i}\nu(r_{ss}+r_{pp})\cot\theta\right] \quad \text{(p-incidence)}, \tag{21a}$$

$$E_r^{\pm} = \frac{1}{\sqrt{2}}\left[-\nu(r_{ss}+r_{pp})\cot\theta \mp \mathrm{i}\left(r_{ss} - \mu\frac{\partial}{\partial\theta} r_{ss}\right)\right] \quad \text{(s-incidence)}. \tag{21b}$$

Substituting Eq. (22) into Eq. (20), the spatial shifts of p- and s-incidences can be achieved, which will be reduced to the well-known result shown in Ref. [33].

3. Numerical results and discussion

The relevant physical parameters for α-MoO_3 film are as follows: along the x direction ([100] crystal direction), $\varepsilon_\infty = 4.0$, $f_{LO} = 972\ \mathrm{cm}^{-1}$, $f_{TO} = 822\ \mathrm{cm}^{-1}$ and $\tau_x = 4\ \mathrm{cm}^{-1}$; along the y direction ([001] crystal direction), $\varepsilon_\infty = 5.2$, $f_{LO} = 851\ \mathrm{cm}^{-1}$, $f_{TO} = 545\ \mathrm{cm}^{-1}$ and $\tau_y = 4\ \mathrm{cm}^{-1}$; along the z direction ([010] crystal direction), $\varepsilon_\infty = 2.4$, $f_{LO} = 1004\ \mathrm{cm}^{-1}$, $f_{TO} = 958\ \mathrm{cm}^{-1}$ and $\tau_z = 2\ \mathrm{cm}^{-1}$. The thickness of the α-MoO_3 film is fixed at $d = 1.3\ \mu\mathrm{m}$. Two typical linearly polarized vortex beams are considered to investigate the spin splitting between LCP and RCP components.

3.1. Spin-splitting for p-incidence

The reflection spectra for LCP and RCP components with varying orientation angle and frequency are illustrated in Figs. 2(a) and 2(b), where we select $w_0 = 40\lambda_0$, $\theta = 45^\circ$ and $m = 1$. From the color bar, it can be seen that the yellow region in the reflection spectra represents higher reflection, while the blue region corresponds to relatively lower reflection. The differences in the reflection spectra are evident for different spin components, where an asymmetric phenomenon is observed in RBs. As shown in Fig. 2(b), the reflection of the RCP component exceeding 50% can be achieved in the range of $\varphi > 20^\circ$ for RB-I and $\varphi < 40^\circ$ for RB-II. However, the reflection of the LCP component in Fig. 2(a) is very small and even approaches zero in the region of $\varphi > 40^\circ$ in RB-II. It is well known that a larger spatial shift generally corresponds to a smaller reflectivity, especially where the reflection is close to zero. In this way, it is possible that this apparent asymmetry of reflectance will lead to a different distribution of the spin splitting with the frequency. Figures 2(c) and 2(d) present the spin splitting for the LCP or RCP component versus the orientation angle and frequency, where the maximum and minimum distribution of spin splitting are obviously related to the reflectance. From the color bar, the red region relates to a larger spin splitting, while the blue region indicates that the spin splitting is small or even tends to zero. In the spin-splitting spectra, the dark blue line indicates that the spin splitting is equal to zero, which means that the spatial shift of LCP and RCP components may be displaced in the same direction and with the same magnitude. The dark red line shows the maximum of the spin splitting due to the spatial shift of LCP and RCP components along the different directions. For example, the in-plane spin splitting can reach $25\lambda_0$, while out-of-plane spin splitting can be $10\lambda_0$. As is evident from a comparison with Figs. 2(a) and 2(b), the maximum value of spatial shift is produced by the LCP component and the minimum value is due to the RCP component.

Next, we simulated the curve of spin splitting as a function of frequency under different incident angles, as shown in Figs. 3(a) and 3(b). Based on Figs. 2(c) and 2(d), we set $\varphi = 45^\circ$, where the maximum of spin splitting can be observed. For in-plane spin splitting, shown in Fig. 3(a), three peaks can be found, located near ENP of RBI and RBII, as well as ENZ of RBIII. The maximum of the spin splitting, about $\Delta x_{max}/\lambda_0 \approx 25$ occurs near ENP of RBII at $\theta = 45^\circ$. A transition between positive and negative spin splitting is achieved at the first peak, with only needing to change the incident angle from 75° to 60°. In addition, the spin splitting is very small when $\theta < 45^\circ$. For out-of-plane spin splitting, a negative maximum of about $\Delta y/\lambda_0 \approx -16.5$ is obtained at $\theta = 60^\circ$ and ENP of RB-I, where a positive maximum of about $\Delta y/\lambda_0 \approx 8.9$ can be observed if the incident angle is set to 75°. The relatively larger spin splitting also can be generated in the other two RBs. With decreasing incident angle, the spin splitting will quickly tend to be zero, especially for $\theta < 30^\circ$. Two cases may cause the spin splitting to be zero. One is when the shifts of both the LCP and RCP components are very small and the other is when the shifts of the LCP and RCP components have the same amplitude and direction although larger shifts are produced. Therefore, if we focus on the polarization of the reflected beam, we have to control the incident angle to be larger than 30°. Of course, if we only hope for large spatial shifts regardless of the polarization of the reflected beam a

smaller incident angle should be also considered. Figures 3(c) and 3(d) present the spin splitting as a function of frequency for different thicknesses of α-MoO_3 at $\varphi = \theta = 45°$. Obvious spin splitting also occurs in or near the RBs, particularly in RB-II near ENP; the maximum of the in-plane spin splitting, about $20\lambda_0$, is observed at $d = 1.3$ μm, and also about $-6.5\lambda_0$ for the out-of-plane spin splitting. In or near RB-I, the spin splitting will move to the lower frequency with increasing thickness; however, in RB-III, the spin splitting will be independent on the thickness of α-MoO_3. From Eq. (10b), a zero reflection will be obtained if $k_{\pm}d = n\pi$, leading to significant spin splitting.

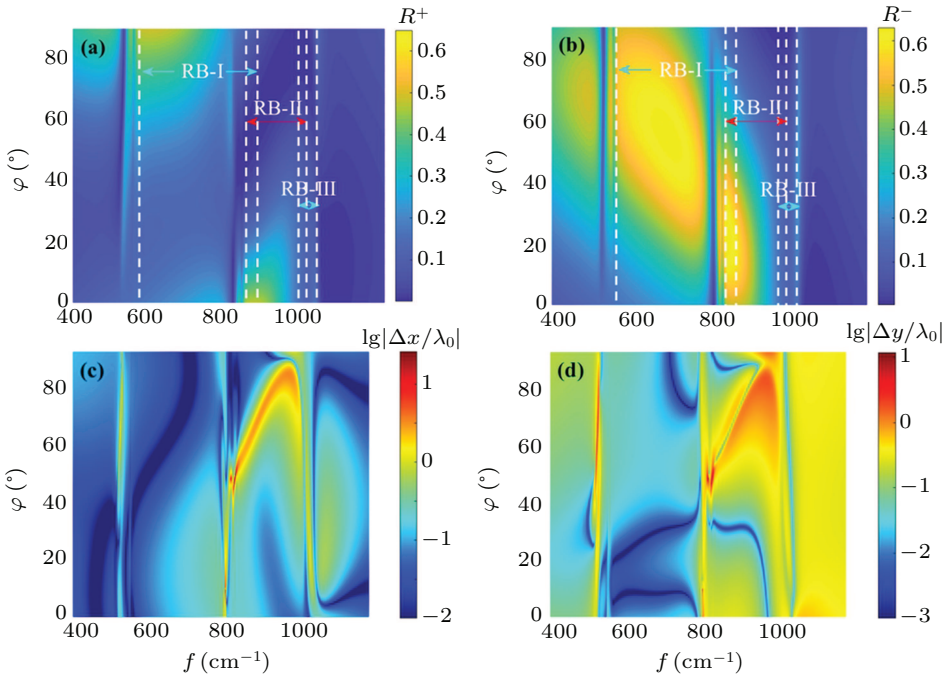


Fig. 2. Reflection of LCP and RCP components in (a) and (b), respectively, versus frequency and orientation angle at $\theta = 45°$ for p-incidence. The yellow region represents higher reflection while the blue region corresponds to relatively lower reflection. The corresponding in-plane and out-of-plane spin splittings are presented in (c) and (d), respectively. To better illustrate the trends, we have utilized a logarithmic coordinate system. The red region is related to a larger spin splitting, while the blue region indicates a small spin splitting close to zero.

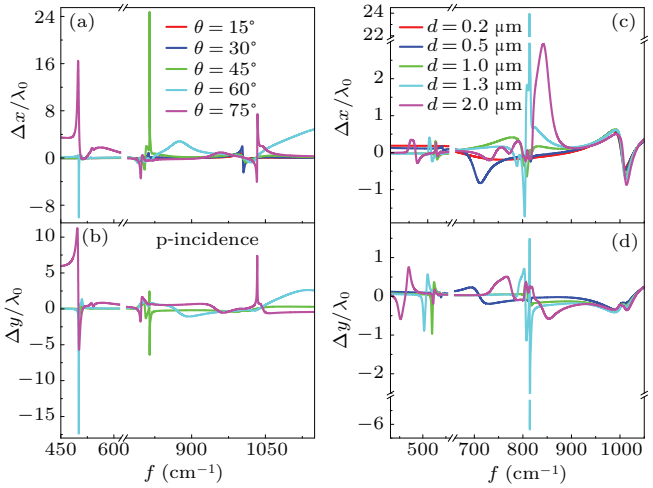


Fig. 3. (a), (b) In-plane and out-of-plane spin splitting for various incident angles at $\varphi = 45°$, respectively. (c), (d) In-plane and out-of-plane spin splitting for various thickness of α-MoO_3 $\theta = \varphi = 45°$, respectively.

In order to more intuitively illustrate the possible relationship between the spatial shifts and the spin splitting produced by LCP and RCP components, Fig. 4 shows the variation of the spatial shifts with frequency under different topological charges. The orientation and incident angles are fixed at $\varphi = \theta = 45°$ since the maximum of spin splitting can be achieved, as shown in Figs. 2 and 3. When a Gaussian beam is incident on the surface of α-MoO_3, namely, $m = 0$, the spatial shifts of LCP and RCP components are also presented. In-plane spatial shifts only can be excited by the LCP components, but the spatial shifts of the RCP components are almost zero. In addition, the spatial shifts generated by the LCP components are located in the three RBs; in particular, the maximum magnitude about $x^+_{\max}/\lambda_0 \approx 33$ at $m = 3$ lies in RB-II, as shown in Fig. 4(b). The inset in Fig. 4(b) further shows that the spatial shifts will increase with increase in topological charge. We can conclude that the spin splitting also will increase with topological charge. The spatial shifts of LCP and RCP components exhibit apparent asymmetry. In this way, we can choose different reflected polarized beams according to the requirements of practical applications. For example, if a zero or tiny spatial shift is anticipated, the RCP component can be selected. However, if a large spatial shift is needed we can consider the LCP component. The out-of-plane spatial shifts in RB-II (see Fig. 4(e)) are complicated and sensitive to the frequency. When $m = 0$, the spatial shifts of the LCP component present two positive peaks and one negative dip. But as the topological charge increases, one of the positive peaks

jumps to the negative one. The positive and negative maxima about $y^{+}_{\max}/\lambda_0 \approx \pm 20$ can be obtained at $\omega = 813$ cm^{-1} and 814 cm^{-1}. Therefore, the direction of the spatial shifts can be adjusted by precisely controlling the incident frequency. In the other two RBs presented in Figs. 4(d) and 4(f), the relatively small spatial shifts that can also be observed are produced by the RCP component. It is obvious that the maximum of spin splitting occurs at the maximum positive and negative spatial shifts, where the spatial shifts of the RCP component disappear.

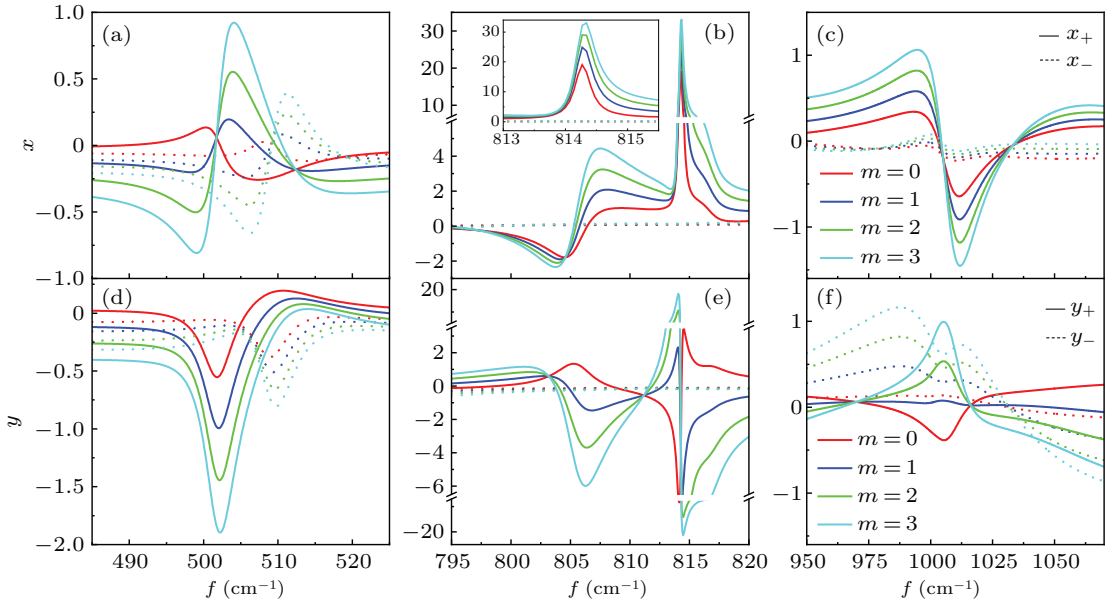


Fig. 4. In- or out-of-plane spatial shifts of the reflected vortex beam for p-incidence under various topological charges at $\varphi = \theta = 45°$.

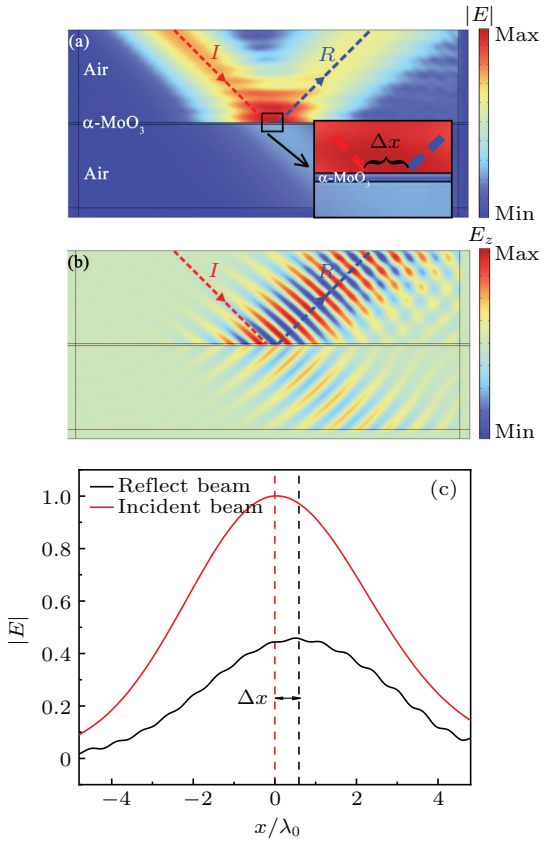


Fig. 5. (a) Electric-field distribution (simulated using the commercial software Comsol Multiphysics) of the p-incidence on the surface of an α-MoO_3 film at $f = 814$ cm^{-1}. The other parameters are the same as those in Fig. 4(b). (b) Distribution of z-components of incident, reflected and transmitted electric fields. (c) Comparison of $|E|$ profiles between the center of the incident and reflected beams.

The simulation results for in-plane spatial shifts using the commercial software Comsol Multiphysics at $m = 0$ for p-incidence with $f = 814$ cm^{-1}are presented in Fig. 5. The center of the reflected beam, marked by the black dotted line, moves obviously to the right along the interface between air and the α-MoO_3 film. In addition, the electric field intensity is significantly enhanced at the interface. According to Fig. 4(b), it can be seen that the in-plane spatial shifts only result from the LCP component, which also can be further reflected through the z-component of electric field in Fig. 5(b). A comparison of the $|E|$ profile between the incident and reflected beams is made in Fig. 5(c). The movement along the x-direction is approximately $x/\lambda_0 \approx 0.8$, which exactly satisfies the theoretical result shown in Fig. 4(b).

3.2. Spin-splitting for s-incidence

The reflective spectra versus frequency and orientation angle of two spin components for s-incidence are shown in Figs. 6(a) and 6(b). Unlike the reflective spectra for p-incidence, the reflection of the LCP component in RB-I and RB-II is obviously larger than that of the RCP component. The maximum of reflection, almost exceeding 50%, lies in the range $20° < \varphi < 70°$ for RB-I and in the range $\varphi > 20°$ for RB-II, as shown in Fig. 6(a). However, the reflection of the LCP component in RB-III achieves a minimum of $R^{+} \approx 0$ once $\varphi > 20°$; in addition, with increasing φ the minimum of the reflection moves to a high frequency and approaches the

right boundary of RB-III. For the reflection of the RCP component shown in Fig. 6(b), the maximum appears near $\varphi = 0°$ for RB-I and $\varphi = 90°$ for RB-II. Similar to the reflective spectra for p-incidence, the reflected intensity exhibits an asymmetric property and varies with the orientation angle. Figures 6(c) and 6(d) present the spin-splitting spectra corresponding to the reflection of the LCP or RCP components, where the asymmetry of the reflectance will result in obvious zero or larger spin splitting. Compared with Figs. 6(a) and 6(b), in or near RB-I and II it can be predicted that the zero spin splitting represented by dark blue lines should originate from the relatively small spatial shifts with the same direction, but the one in RB-III may result from large spatial shifts in the same direction. The dark red lines also represent the distribution of significant spin splitting, which mainly lies in RB-II and RB-III; in addition, at the boundary of these, the maximum of spin splitting can be easily obtained when $\varphi = 0°$ or 90°.

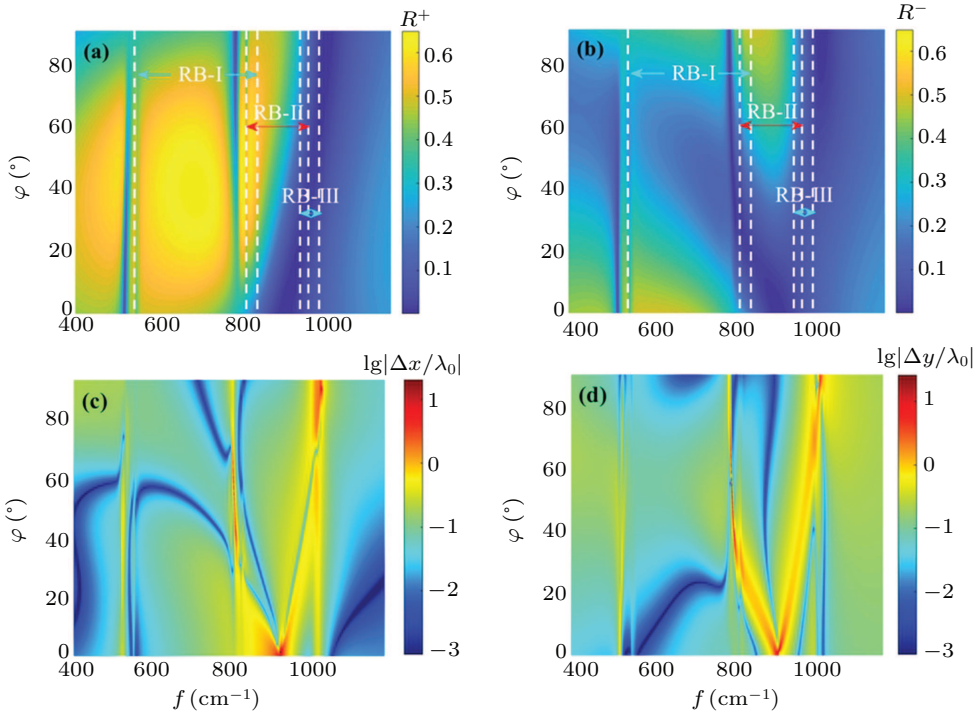


Fig. 6. Reflection of LCP and RCP components in (a) and (b), respectively, versus frequency and the orientation angle at $\theta = 45°$ for s-incidence. The yellow region corresponds to higher reflectance while the blue region corresponds to relatively lower reflectance, approaching zero. The corresponding in-plane and out-of-plane spin splittings are presented in (c) and (d), respectively. To better illustrate the trends, we have utilized a logarithmic coordinate system. The red region corresponds to a larger spin splitting, while the blue region corresponds to a spin splitting close to zero.

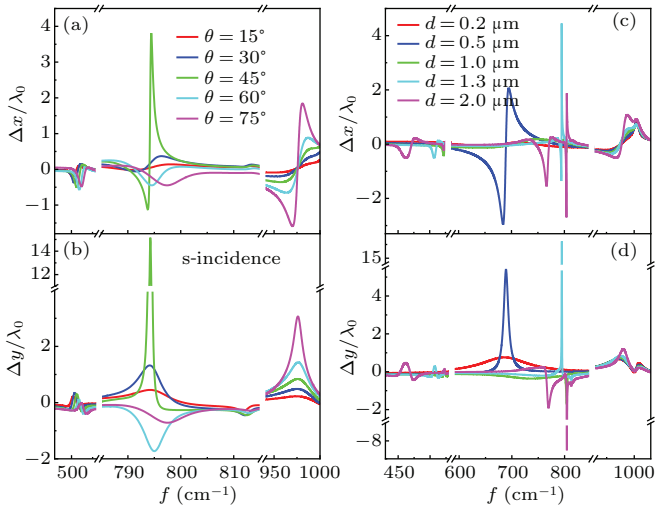


Fig. 7. (a), (b) In-plane and out-of-plane spin splitting for various incident angles at $\varphi = 45°$, respectively. (c), (d) In-plane and out-of-plane spin splitting for various thicknesses of α-MoO_3 at $\theta = \varphi = 45°$, respectively.

The effect of the incident angles for s-incidence on the spin splitting is investigated at $\varphi = 45°$ in Figs. 7(a) and 7(b). For in-plane spin splitting, as shown in Fig. 7(a), three peaks are just consistent with the results in Figs. 2(c) and 2(d). The spin splitting is smaller than that produced by p-incidence, where the positive maximum is about $\Delta x_{max}/\lambda_0 \approx 3.8$ at $\theta = 45°$ and $\omega = 794$ cm^{-1} in RB-II. Another relatively large spin splitting of about $\Delta x_{max}/\lambda_0 \approx 2.0$ at $\theta = 75°$ appears in RB-III. It can be seen that if $\varphi < 45°$, the spin splitting will be less than λ_0 in all the RBs. For out-of-plane spin splitting, as shown in Fig. 7(b), the positive maximum of spin splitting is about $\Delta y_{max}/\lambda_0 \approx 15$ at $\theta = 45°$; obviously is larger than that shown in Fig. 3(b). The negative maximum of spin splitting of about $\Delta y_{max}/\lambda_0 \approx -2$ can be achieved only by changing the incident angle to 60°, which is far from that generated by p-incidence. In RB-III, the spin splitting increases monotonically with increasing incident angle and reaches about $2.5\lambda_0$ at $\theta = 75°$. Therefore, the magnitude and incident frequency of the spin splitting can be adjusted by the incident polarization. As an

example, if the maximum of in- or out-of-plane spin splitting appears in RB-I, we have to choose p-incidence; however, if the maximum occurs in RB-II, s-incidence will be considered. Figures 7(c) and 7(d) show the dependence of the spin splitting on the thickness of α-MoO_3. With increasing thickness, the spin splitting in RB-I and RB-II near ENP increases to a maximum at $d = 1.3$ μm and then decreases again. However, in RB-III near ENZ, the produced spin splitting hardly changes with thickness. It can be found from Fig. 1(b) that the wave vector changes rapidly due to the significant variation of permittivity near ENP, which results in the condition $k_{\pm}d = n\pi$ being easily satisfied. On the other hand, the wave vector in the ENZ region changes more smoothly, which weakens the effect of thickness on spin splitting.

Finally, the in- or out-of-plane spatial shifts of the LCP and RCP components at $\varphi = \theta = 45°$ are presented in Fig. 8. Compared with Fig. 4, the maximum in- and out-of-plane spatial shifts are mainly generated by RCP components in RB-II near ENZ (see Figs. 8(b) and 8(e)). On the contrary, the corresponding spatial shifts of LCP components approach zero. The apparent spin splitting should appear due to the asymmetry of spatial shifts of RCP and LCP components. For an in-plane spatial shift, positive and negative spatial shifts of about $\pm 10\lambda_0$ are achieved at $m = 3$ at $\omega = 794$ cm^{-1} and 795 cm^{-1}. For $m = 0$, a relatively large spatial shift can also be observed in RB-II. In the other two RBs presented in Figs. 8(a) and 8(c), the spatial shifts are relatively smaller. In RB-I, the sign of the maximum spatial shifts excited by LCP and RCP components is opposite, and the magnitude of shifts is less than λ_0. However, in RB-III near ENZ, the positive maximum of about $2\lambda_0$ can be achieved by the LCP component. For out-of-plane spatial shifts, the negative maximum of about $y^{-}_{\max}/\lambda_0 \approx -20$ is observed at $m = 3$ at $\omega = 794$ cm^{-1} and the positive one is about λ_0 at $\omega = 813$ cm^{-1}, as shown in Fig. 8(e). In Figs. 8(d) and 8(f), the spatial shifts are less than λ_0 and the polarized components can be selected according to the requirement for the direction of the spatial shift.

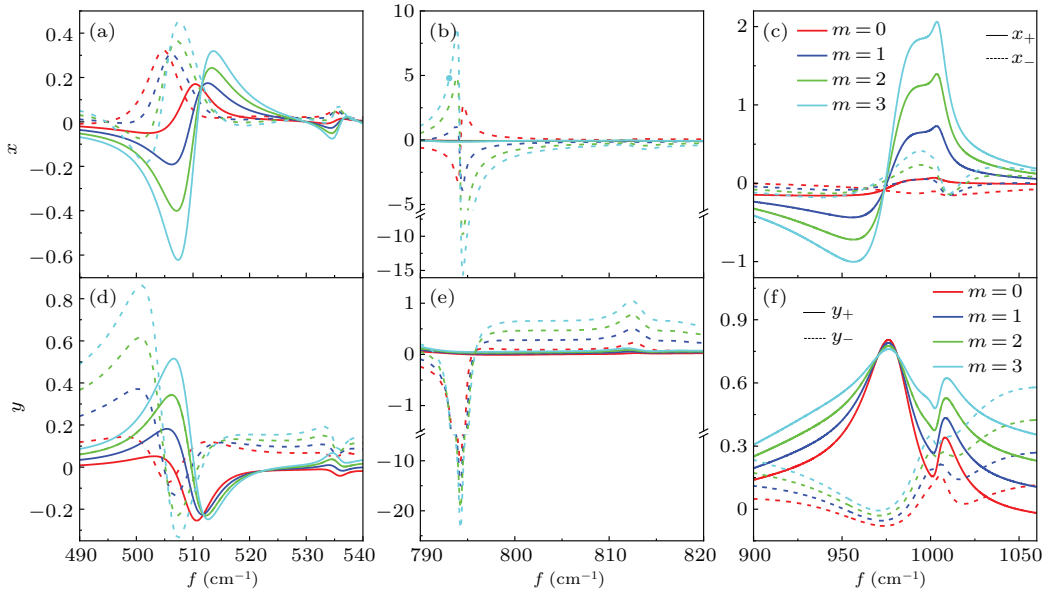


Fig. 8. In- or out-of-plane spatial shifts of the reflected vortex beam for s-incidence under various topological charges at $\varphi = \theta = 45°$.

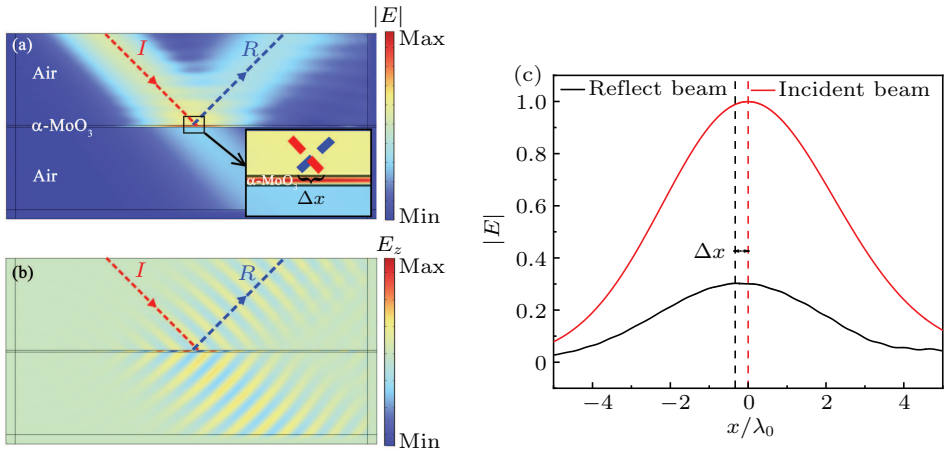


Fig. 9. (a) Electric-field distribution of the s-incidence on the surface of an α-MoO_3 film at $f = 793$ cm^{-1}. The other parameters are the same as those in Fig. 8(b). (b) Distribution of z-components of incident, reflected and transmitted magnetic fields. (c) Comparison of $|E|$ profiles between the center of the incident and reflected beams.

In order to further examine the in-plane spatial shift for s-incidence, Fig. 9 shows the electric field distribution at $m = 0$ with $f = 793\ \mathrm{cm}^{-1}$. Figure 9(a) indicates that the center of the reflected beam moves slightly to the left across the null point along the interface between air and the α-MoO_3 film, which means that a negative spatial shift occurs. The z-component distribution of the magnetic field is presented in Fig. 9(b). Combined with Fig. 8(b), it further demonstrates that the in-plane spatial shifts come from the RCP component due to the zero shift of the LCP component. Finally, the movement of the $|E|$ profile between the incident and reflected beams is about $x/\lambda_0 \approx -0.2$, as shown in Fig. 9(c), which agrees with the calculated value in Fig. 8(b).

4. Summary

In this work we investigated the spin splitting of reflected vortex beams on the surface of an α-MoO_3 film rotated by an angle φ with respect to the incident plane. Two typical polarizations of vortex beams, namely p- and s-incidence, were considered for discussing the spin splitting of LCP and RCP components along the x- and y-directions. The analytical expression for the spatial shifts for the two spin components in the reflective beam was derived, with the spin splitting defined as the shift difference between the two spin components. The sign of the spin splitting indicates the relative positions of the spatial shifts in the xyz coordinate system. We found that obvious spatial splitting normally occurs in the RBs of α-MoO_3 crystal, particularly near ENZ or ENP. For p-incidence, the in- or out-of-plane spin splitting mainly comes from the spatial shift of the LCP component since that of the RCP component approaches zero. However, for s-incidence, in- or out-of-plane spin splitting results from spatial shifts of the RCP component due to the zero shift of the LCP component. The orientation of the optical axis of α-MoO_3 plays an important role in the appearance of the asymmetry. With increasing topological charge, the spatial shifts are greatly enhanced. The effect of the incident angle and the thickness of α-MoO_3 on the spin splitting was also examined, and the optimum incident angle and thickness of α-MoO_3 crystal were determined. The present work may provide a new way for modulating the beam shift and a possibility for developing new tunable anisotropic optoelectronic devices.

Acknowledgement

Project supported by the Natural Science Foundation of Heilongjiang Province of China (Grant No. LH2022F041).

References

[1] Onoda M, Murakami S and Nagaosa N 2004 *Phys. Rev. Lett.* **93** 083901
[2] Bliokh K and Bliokh Y 2006 *Phys. Rev. Lett.* **96** 073903
[3] Shaltout A, Liu J J, Kildishev A and Shalaev V 2015 *Optica* **2** 860
[4] Xiang Y J, Jiang X, You Q, Guo J and Dai X Y 2017 *Photon. Res.* **5** 467
[5] Guddala S, Khatoniar M, Yama N, Liu W X, Agarwal G S and Menonet V M 2021 *Optica* **8** 50
[6] Zhou X X, Zhang J, Ling X H, Chen S Z, Luo H L and Wen S C 2013 *Phys. Rev. A* **88** 053840
[7] Zhang Q, Gao D L and Gao L 2021 *Opt. Express* **29** 9816
[8] Bai X X, Tang L L, Lu W Q, Wei X Z, Liu S and Liu Y 2017 *Opt. Lett.* **42** 4087
[9] Zhang W S, Wu W J, Chen S Z, Zhang J, Ling X H and Shu W X 2018 *Photon. Res.* **6** 511
[10] Prinz E, Hartelt M, Spektor G, Orenstein M and Aeschlimann M 2023 *ACS Photonics* **10** 340
[11] Efremidis N K, Chen Z G, Segev M and Christodoulides D N 2019 *Optica* **6** 686
[12] Stoian R, Bhuyan M K, Zhang G D, Cheng G H, Meyer R and Courvoisier F 2018 *Adv. Opt. Techn.* **7** 165
[13] Nye J F and Berry M V 1974 *Proc. R. Soc. Lond. A* **336** 165
[14] Yan Y, Xie G D, Lavery M P J, Huang H, Ahmed N, Bao C J, Ren Y X, Cao Y W, Li L, Zhao Z, Molisch A F, Tur M, Padgett M J and Willner A E 2014 *Nat. Commun.* **5** 4876
[15] Gahagan K T and Swartzlander G A 1996 *Opt. Lett.* **21** 827
[16] Yan L, Gregg P, Karimi E, Rubano A, Marrucci L, Boyd R and Ramachandran S 2015 *Optica* **2** 900
[17] Zhu W G, Jiang M J, Guan H Y, Yu J H, Lu H H, Zhang J and Chen Z 2017 *Photon. Res.* **5** 684
[18] Chen Z, Zhang H, Zhang X, Li H, Yang J X, Zhang W B, Xi L X and Tang X F 2020 *Opt. Express* **28** 29529
[19] Liu R, Wang G H, Deng D M and Zhang T T 2021 *Opt. Express* **29** 22192
[20] He Y, Xie Z, Yang B, Chen X, Liu J, Ye H, Zhou X, Li Y, Chen S and Fan D 2020 *Photon. Res.* **8** 963
[21] Haug J, Palei M and Shrout J D 2021 *Opt. Express* **29** 42331
[22] Liu X Z, Kong W J and Wang C T 2021 *J. Appl. Phys.* **54** 285103
[23] Argyropoulos C, Estakhri N M, Monticone F and Alù A 2013 *Opt. Express* **21** 15037
[24] Fu J C, Jin Y, Evans J and He S L 2020 *Adv. Photon. Res.* **2** 2000043
[25] Dai S, Ma Q, Andersen T I, Mcleod A S, Fei Z, Liu M K, Wagner M, Watanabe K, Taniguchi T, Thiemens M, Keilmann F, Jarillo-Herrero P, Fogler M M and Basov D N 2015 *Nat. Commun.* **6** 6963
[26] Vasilantonakis, Wurtz G A, Podolskiy V A and Zayats A V 2015 *Opt. Express* **23** 14329
[27] Li P N, Dolado I, Alfaro-Mozaz F J, Casanova F, Hueso L E, Liu S, Edgar J H, Nikitin A Y, Vélez S and Hillenbrand R 2018 *Science* **359** 892
[28] Kim H S, Cook J B and Lin H 2017 *Nat. Mater.* **16** 454
[29] Ma W L, Alonso-González P and Li S J 2018 *Nature* **562** 557
[30] Sheng D, Gao A, Liu X and Zhang Q 2023 *Nanomaterials* **13** 2272
[31] Zheng Z B, Xu N S, Oscurato S L, Tamagnone M, Sun F S, Jiang Y Z, Ke Y L, Chen J N, Huang W C, Wilson W L, Ambrosio A, Deng S Z and Chen H J 2019 *Sci. Adv.* **5** eaav8690
[32] Hu G W, Ou Q D, Si G Y, Wu Y J, Wu J, Dai Z G, Krasnok A, Mazor Y, Zhang Q, Bao Q L, Qiu C W and Alù A 2020 *Nature* **582** 209
[33] Song H Y, Wang X G, Hao S P, Fu S F and Wang X Z 2023 *Opt. Commun.* **542** 129603
[34] Zhou S, Khan A, Fu S F and Wang X Z 2018 *Opt. Express.* **27** 15222
[35] Deng G S, Dereshgi S A, Song X L, Wei C W and Aydin K 2020 *Phys. Rev. B* **102** 035408
[36] Peng H Y and Wang X Z 2021 *J. Opt. Soc. Am. B* **38** 2027
[37] Bliokh K Y and Aiello A 2013 *J. Opt.* **15** 014001